

Imaging the Earth's Magnetosphere: Effects of Plasma Flow and Temperature

D.E. GARRIDO, R.W. SMITH, D.S. SWIFT, S-I. AKASOFU

Geophysical Institute and Department of Physics, University of Alaska-Fairbanks, Fairbanks, AK. 99775-0800, U.S.A.

(Camera-ready copy received in final form 21 August 1991)

We simulate EUV images of the magnetosphere at 83.4 nm for cases where the plasma has a non-zero drift velocity with respect to the sun and variable plasma temperature. The solar emission in this region is dominated by a blend of nine gaussian shaped lines representing the O^+ triplet and the O^{++} sextuplet contributions, (Meier, 1990a). The magnetospheric scattering cross-section profile includes only contributions from the O^+ triplet due to the low number density of O^{++} compared to that of O^+ , (Chandler, 1987). The scattering rate has a complicated structure as a function of bulk velocity and does not possess any symmetry about zero. The scattering rate is reduced for most Doppler shifted cases compared to the case of zero bulk velocity, resulting in a much dimmer image. At some bulk velocities where the scattering cross-section of O^+ peaks at the brighter O^{++} solar line profiles, larger scattering rates occur and the EUV image is brighter. Similarly, due to thermal Doppler spread the scattering rate decreases with increasing plasma temperature. Using a simple model for the O^+ ion number density we present simulated images of the magnetosphere including the radiation belt and plasma sheet for different viewing positions at distances of the order of 50 R_e from the earth. We show that an EUV magnetospheric image of minimum reasonable quality may be obtained in 1000 s using an electronic imager with an aperture of 750 cm². Several comparative cases are shown to illustrate the simulated images in different perspectives and for a selection of bulk plasma velocities and temperatures.

1. INTRODUCTION

The experimental study of the magnetosphere has proceeded by a process of assembly and careful correlation of point measurements of fields and particles made by satellite instruments in the various plasma regions. Seldom has it been possible to gather an extensive data set for a single geometry or instant in magnetospheric time and space. The contextual information needed to make best use of point measurements of the plasma could be found in an image of the plasma region made optically (Johnson et al., 1971, Meier, 1990b, Swift et al., 1989, Chiu et al., 1990) and complementarily by the use of energetic neutral particles, (Roelof, 1989). Imaging by optical means gives more information on the lower energy component of the plasma particle population while the energetic neutral particle technique depends upon the higher energy component.

The sun provides a stream of photons which may be scattered by the ions in the magnetosphere. This scattering is most effective at wavelengths where there is a strong ionic resonance, such as 30.4 nm for He^+ and the triplet at 83.4 nm for O^+ . The scattered light enables the observer to determine the shape and position of regions of the magnetosphere where these ions are found and the absolute intensity in any direction gives the line-of-sight column density of the scatterer. This paper is concerned with possible 83.4 nm images of the O^+ densities since information gain from these can be used to study the ionosphere and the magnetosphere. The O^+ found in the magnetosphere can be assumed to have originated in the ionosphere and to have been advected by the action of coupling processes which link the magnetosphere and the ionosphere.

Swift et al., 1989 and Chiu et al., 1990 showed examples of images at 83.4 nm simulated by computer. Regions of higher density of O^+ in the plasmasphere and plasma sheet show up brighter than their surroundings. In addition, Chiu et al., 1990 show that the ion outflow from the polar caps should

also become visible. In both of these earlier papers, no allowance has been made for reduction in scattering efficiency due to high plasma temperature or fast plasma streaming. This paper addresses both these topics giving more realistic simulations of a magnetospheric image and also updated estimate on the imager aperture required for a reasonable frame rate for pictures taken from the moon.

The calculation of the g-factor, expressing the scattering rate of solar emission in photons/s/ion has been done by (Meier, 1990a) for the 83.4 nm region that incorporates the correct blend of O^+ and O^{++} transitions. The well resolved solar intensity profile is composed of an O^+ triplet and an O^{++} sextuplet. The fractional distribution, b , of the solar intensity into the respective emission lines has also been calculated by (Meier et al., 1991) and shown to be $b=0.26$ for O^+ and $b=0.74$ for O^{++} . In analyzing the effects of plasma drifts on the cross-section of the ions, the analysis of the scattering rate as a function of bulk velocity, (Meier, 1990a) requires an understanding of how the shift in the cross-section line center can affect the scattering rate and thus produce its structure. Due to close spacing and intermixing of the O^+ and O^{++} lines, a non-zero bulk velocity of the O^+ ions can result in an O^+ cross-section profile overlapping with another line in the O^+ triplet or with a line of the O^{++} sextuplet. An O^+ ion having the right drift speed can resonantly scatter photons emitted from an O^{++} ion. Since some lines in the O^{++} spectrum are much more intense than those in the O^+ triplet, enhanced scattering can occur. This idea is discussed in detail in a later section. We analyze the structure of the scattering rate as a function of bulk and random velocity by assuming that the cross-section profile for the 83.4 nm wavelength contains only the O^+ triplet.

It will be of great interest to observe the marked changes in the magnetospheric image, say, of the plasma sheet during a substorm by comparing an image observed during 'quiet' times with images obtained during disturbed conditions identified with a marked increase in O^+ number density (Lennartson et al., 1986).

2. BRIEF REVIEW OF ATOMIC AND SOLAR DATA

Fig. 1 shows the energy level diagram corresponding to the O^+ triplet and the O^{++} sextuplet transition, (Ho and Henry, 1983). The solar flux I_0 , (Hinterreger, 1981) has a magnitude of $.67 \times 10^9 \text{ photons cm}^{-2} \text{ s}^{-1}$ and the branching ratios p_n that distribute the solar flux into the nine solar lines can be obtained in terms of the statistical weights of the upper levels of the transitions and also in terms of the Einstein coefficients A_{ln} (for spontaneous emissions to the lower energy levels). The branching ratio p_n is defined by

$$p_n = \frac{w_n}{\sum_i w_i} \frac{A_{ln}}{\sum_l A_{ln}} b_n \quad (1)$$

where

$$\frac{w_n}{\sum_i w_i} = \text{relative strength of statistical weights} \quad (2-a)$$

$$\frac{A_{ln}}{\sum_l A_{ln}} = \text{relative Einstein coefficients} \quad (2-b)$$

and

$$b_n = .26 \text{ for } n = 1, 3 \text{ (the } O^+ \text{ lines)} \quad (3a)$$

$$b_n = .74 \text{ (the } O^{++} \text{ lines) for } n = 4, 9 \quad (3b)$$

The absorption cross section at line center (ν_{0i}) (see Appendix) is given by

$$\sigma_{0i} = \sigma_i \frac{c}{u_i \nu_{0i} \sqrt{\pi}} \quad (4)$$

and is temperature dependent through the thermal speed, $u_i = \sqrt{2kT/m_o}$ of the ions.

The integrated cross-section is defined as

$$\sigma_i = \frac{\pi e^2}{m_e c} f_i \quad (5)$$

Table 1: Solar line and atomic data

$\lambda(\text{nm})$	$\nu(10^{15} \text{ Hz})$	J_u	w_u	$\frac{w_u}{\sum_u w_u}$	$A_{lu}(10^8/\text{s})$	$\left(\frac{A_{lu}}{\sum_l A_{lu}}\right)N$	f_i	p_i	$\sigma_{0i}(\text{cm}^2)$
83.4462	3.59513	5/2	6	6/12	7.6	.93	.122	.121	$1.5e-13$
83.3326	3.60003	3/2	4	4/12	8.2	1.0	.0872	.086	$1.1e-13$
83.2754	3.60250	1/2	2	2/12	8.2	1.0	.041	.043	$5.0e-14$
83.2927	3.60175	1	3	3/15	3.3	.59	.102	.087	
83.3742	3.59823	2	5	5/15	4.3	.77	.0748	.189	
83.5096	3.59240	2	5	5/15	1.4	.25	.015	.061	
83.5292	3.59155	3	7	7/15	5.6	1.0	.0816	.345	
83.3715	3.59835	1	3	3/15	2.3	.41	.0245	.061	
83.5059	3.59256	1	3	3/15	.16	.03	.001	.0044	

Energy Level Diagram

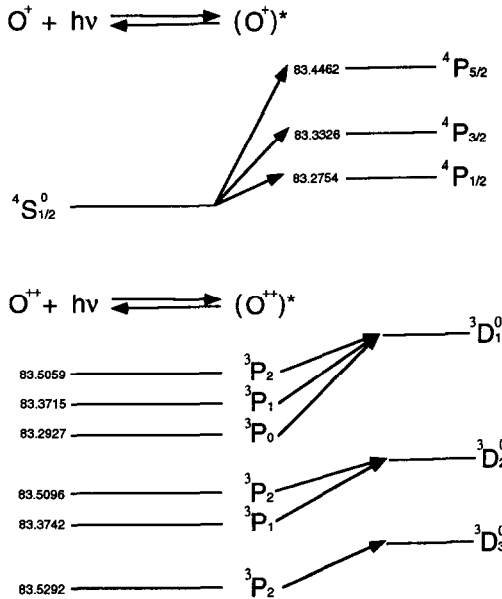


Fig. 1 Table of Solar and Atomic Data as adopted from Meier (1990a). Energy level diagrams are shown explicitly to describe the relevant transitions.

where

$$\int_0^\infty \sigma_i^a(\nu) d\nu = \sigma_i \quad (6)$$

where $\sigma_i^a(\nu)$ is the cross-section profile for a particular transition and f_i is the oscillator strength. Measured values for the cross-section at line center for O^+ are given by (Kumar et al., 1983) for $T_i=1000$ K. The values for the cross-section obtained using (4) are shown in the last column of the table in Fig. 1. The scattering rate at other temperatures were obtained using equations (5) and (6).

3. ANALYSIS OF THE SCATTERING RATE g

The theory relevant to the calculation of the g -factor (photons/s/ion) is discussed in (Meier, 1990a). Although the method of analysis is familiar we describe it briefly in the Appendix. Our purpose is to clarify the normalization constants used in our computations. Even though we use the same data, we have obtained slight differences in the values calculated for g . The difference may lie in the temperatures of the ions in the chromosphere. For O^+ we have used $T_1=50000$ K and for O^{++} $T_2=130000$ K, yielding a gaussian width of .0033 and .0047 nm, respectively. This compares to the value of .0039 and .0054 nm obtained by (Meier et al., 1991). Neglecting background light and the effects of solar rotation, the solar line profiles are assumed to be of the form

$$I(\nu) = \sum_{n=1}^9 I_n \kappa_{0n} e^{-\frac{c^2}{u_n^2 \nu_{0n}^2} (\nu - \nu_{0n})^2} \quad (7)$$

where

$$I_n = I_0 p_n \quad (8-a)$$

$$\kappa_{0n} = \frac{c}{u_n \nu_{0n} \sqrt{\pi}} \quad (8-b)$$

and the Doppler shifted cross-section profile is given by

$$\sigma_d^a(\nu) = \sum_{m=1}^3 \sigma_m \kappa_{0m} e^{-\frac{c^2}{u_m^2 \nu_{0m}^2} (\nu - \nu_m)^2} \quad (9)$$

where

$$\nu_m = \nu_{0m}(1 + v_p/c) \quad (10-a)$$

$$\kappa_{0m} = \frac{c}{u_m \nu_{0m} \sqrt{\pi}} \quad (10-b)$$

The subscript n labels quantities of chromospheric origin while m identifies magnetospheric quantities and v_p is the bulk velocity. Our calculations show that the g factor for the case $v_p = 0$ is 2.45×10^{-7} and 2.67×10^{-7} photons/s/ion for plasma temperatures of 1 keV and 10 keV, respectively. This represents an average value which will fluctuate with solar activity. The plot of scattering rate v.s. drift speed is shown in Fig. 2. The complex structure of the g factor shows regions of v_p where g has a significant value and others where it is relatively small.

We analyze both cases where negative drift speeds cause the shifting of the cross-section line centers towards larger wavelengths while positive drift speeds shift the line centers to smaller wavelengths. The varying overlap of the profiles explains the structure of the g factor. The nature of the cross-section and the near resonance of the transitions at 83.4 nm determine the structure of the scattering rate. One can read from Fig. 2 the drift speeds at which the g factor is small or large, thus enabling us to infer whether our magnetospheric image is dark or bright. The temperature dependence of g is shown in Fig. 2 and the effects on the mag-

G FACTOR FOR O^+ VS DRIFT SPEED

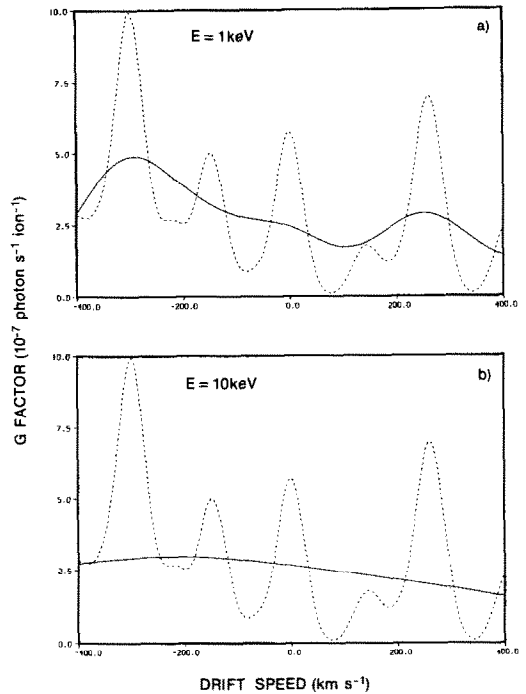


Fig. 2a-2b Plots of the g -factor as a function of ion drift velocity. In all cases the dashed curve refers to the case when the plasma temperature $T=100$ eV. (a) The solid curve represents the $T=1$ keV case. (b) The solid curve represents the $T=10$ keV case.

netospheric images are shown in Fig. 6. We will discuss the results of the simulations on the images in a later section. As the temperature is increased the absorption cross-section is broadened preserving the total area constant. Fig. 2 shows and compares the variation of the scattering rate with drift velocity at various plasma temperatures. The dashed curve represents the structure of the scattering rate when $T=100$ eV and the solid line represent the case when $T=1$ keV or $T=10$ keV. For the case when $T=1$ keV we see that the scattering rate has a peak around -300 km s^{-1} . The minus sign means that the flow velocity is anti-sunward. Positive velocities will mean that the ion velocities are directed towards the sun. The value of the scattering rate is seen to decrease as we go towards positive drift speeds up until 100 km s^{-1} where it starts to increase. Another peak in the scattering rate is obtained at speeds of about 300 km s^{-1} . The Doppler effects caused by the ion flow velocities are shown in Fig. 4 and Fig. 5. The case when $v_p=-300 \text{ km s}^{-1}$ indicates a maximum value for the scattering rate when $T=1$ keV and this results in a relatively brighter image.

4. SIMULATION OF MAGNETOSPHERIC IMAGES USING O^+ EMISSIONS

Simulations of global images of the magnetosphere were obtained by (Swift et al., 1989) by using resonantly scattered emissions from O^+ ions in the 83.4 nm wavelength band. The images obtained were based on a higher value of

the scattering rate than that used here in our simulations. They used a simple model for the O^+ number density and an asymmetric radiation belt on dipole magnetic field lines. However, the global features of the magnetosphere that depend on plasma bulk velocity and temperature variations were not analysed. Due to the inavailability of data on a well resolved solar profile, it was difficult to ascertain the correct line shapes to use in the simulations so that temperatures of the ions in the chromosphere were taken to be of the order of 10^4 K thus using a width that is much smaller than that used in this paper. In this section, we incorporate the effects of temperature variation and plasma drift speeds on the magnetospheric images. Our model assumes a symmetric dipole field where the geographic and magnetic coordinates coincide. The equation for the magnetic lines of force is given by (Roederer, 1970),

$$r = r_0 \cos^2(\lambda) \quad (11)$$

where r_0 is a constant of integration and λ is the magnetic latitude. If we let

$$r_0 = LR_e \quad (12)$$

where (R_e =earth radii), and L the distance of the field line at equatorial crossing in units of Earth radii, we obtain

$$R = r/R_e = L \cos^2(\lambda) \quad (13)$$

The lines of force intersect the surface of the earth at latitudes given by

$$\cos(\lambda_e) = 1/\sqrt{L} \quad (14)$$

The radiation belt is assumed to extend from $L=3$ to $L=15$ with a density profile that varies as

$$n = 1/L \text{ (ions cm}^{-3}\text{)} \quad (15)$$

with a uniform plasma temperature of 10 keV. By assuming the radiation belt to extend between L values of 3 and 15 we have neglected contributions coming from the plasmasphere. The form of the density profile and the extent of the radiation belt is a crude assumption used to illustrate the dipole structure present in the magnetospheric image as illustrated in Fig. 3 Case 1 which is discussed below. Uniform L shell populations have been imposed without regard to any redistribution which might occur due to subsequent motions. The plasma sheet is assumed to have the ellipsoidal form

$$\frac{(x+20)^2}{(20)^2} + \frac{y^2}{(15)^2} + \frac{z^2}{(3)^2} = 1 \quad (16)$$

with a uniform density of $.1 \text{ cm}^{-3}$, (Lennartson *et al.*, 1986).

The contributions of the ionospheric plasma are blanked out because the ion number densities are much larger than those in the radiation belts and plasma sheet, thus enabling us to view the dimmer portions of the magnetosphere. We assume that the earth hides the plasma behind it from the sun. In describing our simulation images we denote the satellite positions by cartesian solar magnetospheric coordinates (X_0, Y_0, Z_0) measured in Earth radii. The positive X axis points in the sunward direction and the Z axis is perpendicular to the solar ecliptic plane. The view direction is denoted by coordinates ($X_1, 0, 0$). The view direction is represented by a vector directed from the observer's position towards the point ($X_1, 0, 0$).

In Fig. 3a-3d we show the grey scale images of the magnetosphere for four different satellite positions. Frame (a) Case 1, is described by the coordinates ($X_0=20, Y_0=0, Z_0=0$)

with view direction at ($X_1=0$). Frame (b) Case 2, is described by coordinates ($X_0=20, Y_0=5, Z_0=-50$) also viewing at $X_1=10$. Another look at the magnetosphere is shown in frame (c) Case 3 and frame (d) Case 4 which are described by coordinates ($X_0=0, Y_0=-10, Z_0=-50, X_1=-10$) and ($X_0=20, Y_0=10, Z_0=40, X_1=10$), respectively.

In Fig. 3 frame (a) defines Case 1 indicating that the observer with coordinates (20,0,0) (measured relative to the center of the Earth) is located at 20 Earth radii on the sunward side and viewing directly towards the center of the earth. We assume that when the picture of the magnetosphere was taken the radiation belt ions have a temperature of 10 keV while the ions in the plasma sheet have $T=1$ keV. The drift velocities are assumed to be zero in both regions. The central hollow represents the earth with a small contribution coming from extensions of the radiation belt towards the dayside. The relative brightness seen in the image decreases symmetrically along the dawn to dusk direction. The brightest portions of the ring currents begin at $L=3$ and the gradual decrease in brightness as we go away from the Earth is governed by the density profile of equation (15). The maximum image brightness obtained is approximately 1.33×10^{-3} Rayleighs. For Cases 2-4 we have also assumed the same temperature and velocity conditions for the radiation belt and plasma sheet. The grey scale bar uses a maximum intensity of 1.33×10^{-3} Rayleighs and refers to Fig. 3a.

Another view of the magnetosphere is shown in Fig. 3 frame (b) defining Case 2. The observer is located at (20,5,-50). The view direction ($X_1=10$) means that the satellite is looking at a distance 10 R_e behind the Earth in the magnetotail. For this view the maximum image brightness is 3.49×10^{-4} Rayleighs. The grey scale maximum of 4.19×10^{-4} Rayleighs is used in this case and all other cases discussed below. The radiation belt appears to have a spherical configuration. The sunward portions of the belt appears less brighter than portions tailward and the plasma sheet is dim in contrast to the radiation belt. Frames (c) and (d) represent two other viewing perspectives of the magnetosphere. The maximum image brightness are 3.28×10^{-4} and 3.74×10^{-4} Rayleighs, respectively.

The different views of the magnetosphere shown in Fig. 3 allow us to view both the radiation belt and the plasma sheet. The shadowing of the plasma behind the earth from sunlight is seen to start with a central dark spot representing the earth and a dim region continuing straight down the magnetotail. The slightly enhanced brightness towards the night side is because the radiation belt and the ellipsoidal plasma sheet overlap and contributions from both regions are additive.

Effects of Doppler Shift

In Fig. 4-5 we show how the magnetospheric image varies with changing drift speed for the view direction representing Case 4. In our model we assume that only ions in the plasma sheet are drifting while there are no plasma drifts occurring in the radiation belt. The temperature of the radiation belt ions is 10 keV and the plasma sheet ions has $T=1$ keV. Fig. 4 frame (a) represents the image when $v_p=0$ (b) $v_p=-100 \text{ km s}^{-1}$ (c) $v_p=-200 \text{ km s}^{-1}$ (d) $v_p=-300 \text{ km s}^{-1}$. We can see that as the drift velocities increase in the anti-sunward direction the plasma sheet appears to brighten gradually and begin to show more structure. The enhanced brightness can be explained by Fig. 2. The scattering rates for the four cases above are 2.4×10^{-7} , 2.8×10^{-7} , 3.9×10^{-7} and 4.9×10^{-7} photons/s/ion, respectively. Since the scattering rate at -300 km s^{-1} is largest the image will

PLASMA SHEET ($T = 1 \text{ keV}$, $V_p = 0$), RADIATION BELT ($T = 10 \text{ keV}$, $V_p = 0$)

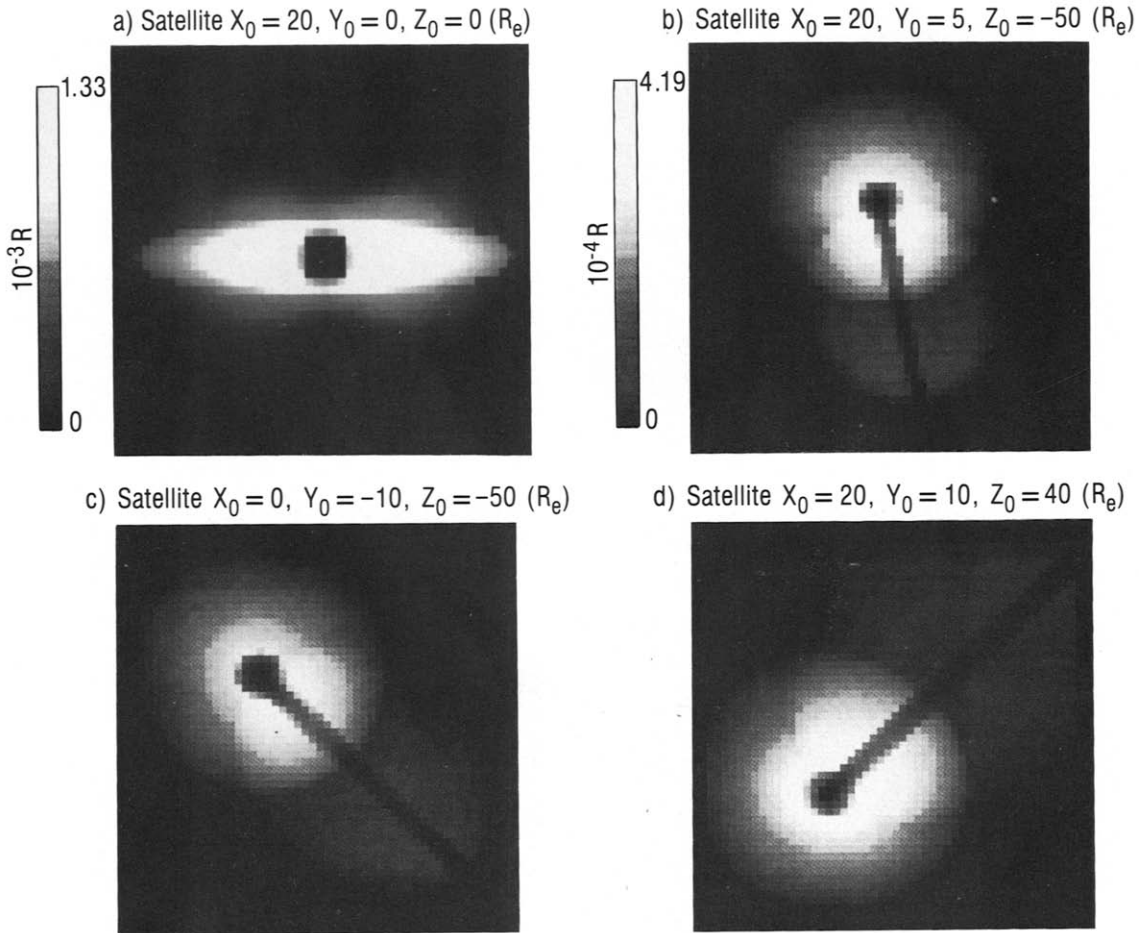
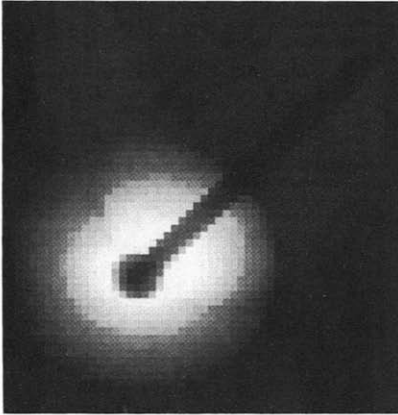


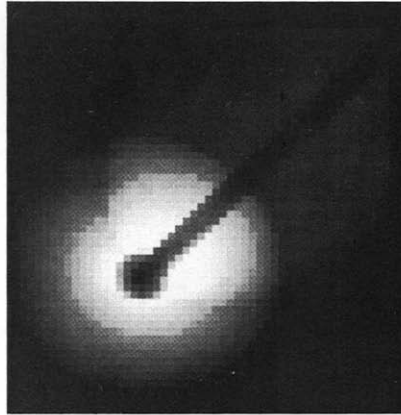
Fig. 3a-3d Magnetospheric images for different satellite positions and view directions. The ions in the radiation belt are assumed to have a temperature and flow velocity of $T=10 \text{ keV}$ and $v_p=0$ while in the plasma sheet $T=1 \text{ keV}$ and $v_p=0$. The following cases are described Frame (a) Case 1 (b) Case 2 (c) Case 3 (d) Case 4. The different cases are defined in Section 4.

**PLASMA SHEET ($T = 1 \text{ keV}$, $V_p = \text{antisunward}$),
RADIATION BELT ($T = 10 \text{ keV}$, $V_p = 0$)**

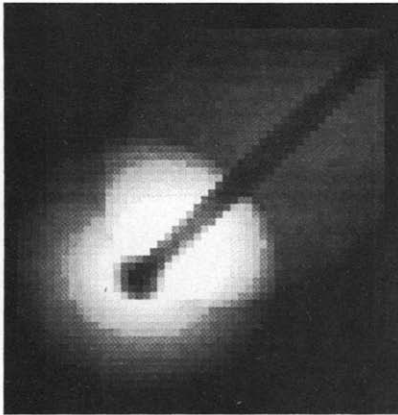
a) Plasma Sheet ($V_p = 0$)



b) Plasma Sheet ($V_p = -100 \text{ kms}^{-1}$)



c) Plasma Sheet ($V_p = -200 \text{ kms}^{-1}$)



d) Plasma Sheet ($V_p = -300 \text{ kms}^{-1}$)

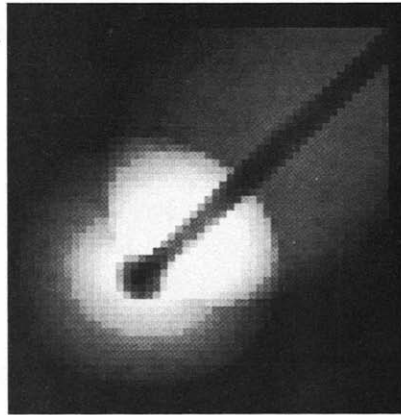
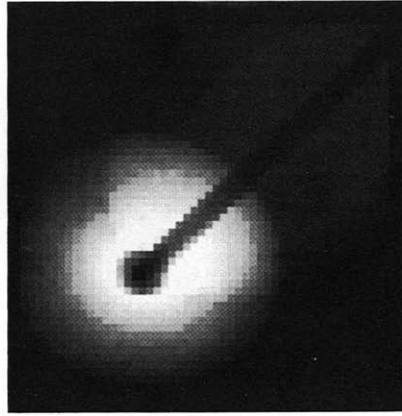
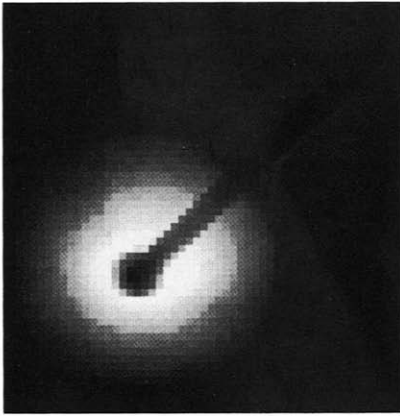


Fig. 4a-4d Case 4 show variation of the magnetospheric image when the plasma sheet ions have an anti-sunward flow velocity v_p . Its temperature is assumed to be 1 keV. The drift velocities are given by Frame (a) $v_p = 0$ (b) $v_p = -100 \text{ km s}^{-1}$ (c) $v_p = -200 \text{ km s}^{-1}$ (d) $v_p = -300 \text{ km s}^{-1}$. The ions in the radiation belt are assumed to have $T = 10 \text{ keV}$ and $v_p = 0$.

PLASMA SHEET ($T = 1 \text{ keV}$, $V_p = \text{sunward}$),
RADIATION BELT ($T = 10 \text{ keV}$, $V_p = 0$)

a) Plasma Sheet ($V_p = 100 \text{ kms}^{-1}$) b) Plasma Sheet ($V_p = 200 \text{ kms}^{-1}$)



c) Plasma Sheet ($V_p = 300 \text{ kms}^{-1}$) d) Plasma Sheet ($V_p = 400 \text{ kms}^{-1}$)

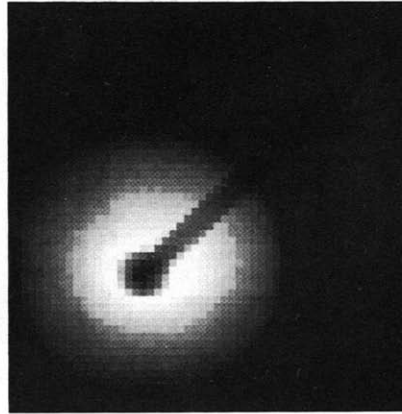
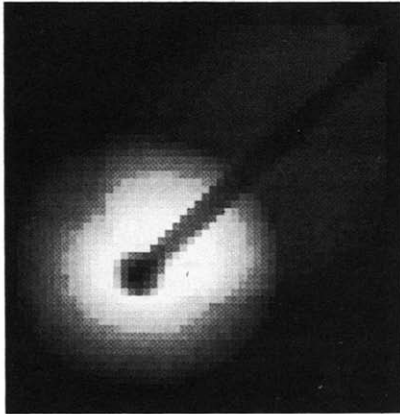
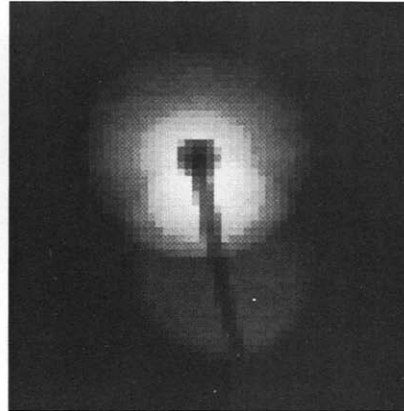
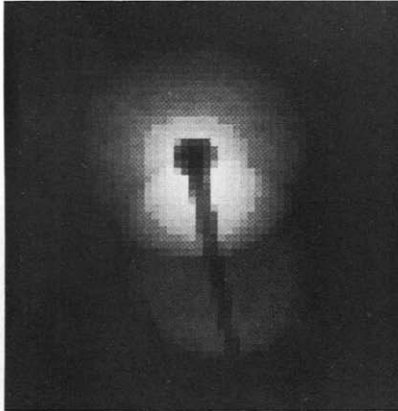


Fig. 5a-5d Case 4 show variation of the magnetospheric image when the plasma sheet ions have a positive (sunward) flow velocity v_p . The ions are assumed to have $T=1 \text{ keV}$. The drift velocities are given by Frame (a) $v_p=100 \text{ km s}^{-1}$ (b) $v_p=200 \text{ km s}^{-1}$ (c) $v_p=300 \text{ km s}^{-1}$ (d) $v_p=400 \text{ km s}^{-1}$

PLASMA SHEET ($T = 1 \text{ keV}$, $V_D = 0$), RADIATION BELT ($V_D = 0$)

a) Radiation Belt ($T = 1 \text{ keV}$)

b) Radiation Belt ($T = 4 \text{ keV}$)



c) Radiation Belt ($T = 8 \text{ keV}$)

d) Radiation Belt ($T = 10 \text{ keV}$)

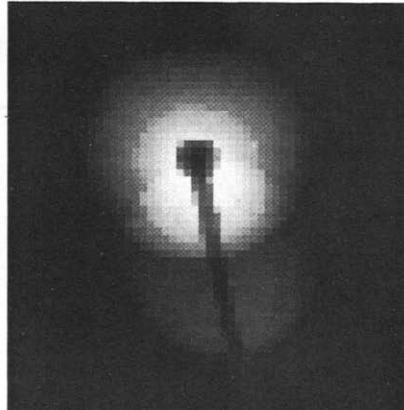
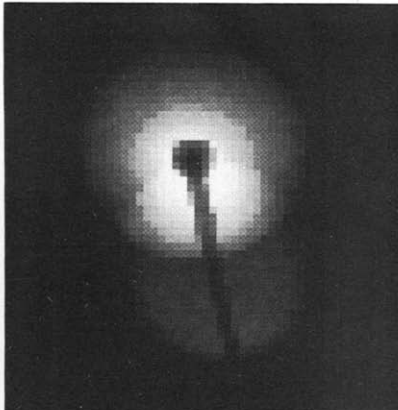
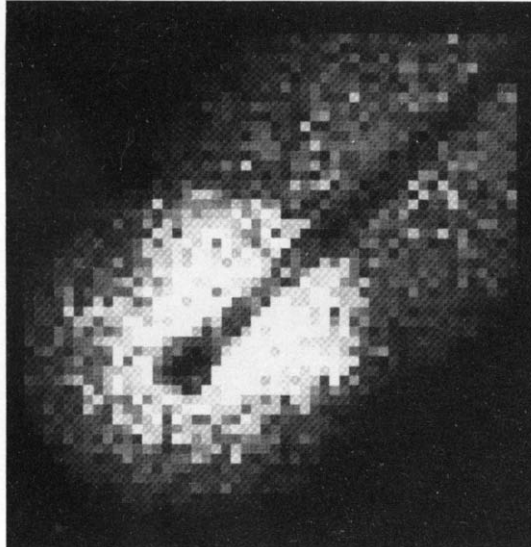


Fig. 6a-6d Case 2 show effects of temperature broadening on the magnetospheric image. The plasma sheet ions are assumed to have a plasma temperature and flow velocity of $T=1 \text{ keV}$ and $v_p=0$ while in the radiation belt the temperature is allowed to vary. Frame (a) $T=1 \text{ keV}$ (b) $T=4 \text{ keV}$ (c) $T=8 \text{ keV}$ (d) $T=10 \text{ keV}$. The flow velocity in the radiation belt is taken to be zero.

PLASMA SHEET ($T = 1 \text{ keV}$, $V_p = 0$)
RADIATION BELT ($T = 10 \text{ keV}$, $V_p = 0$)



Mirror area = 750 cm^2

Image randomized for Poisson counting distribution

Fig. 7 Case 4. The image quality of the radiation belt and plasma sheet as seen with an aperture size of 750 cm^2 . The radiation belt ions have $T=10 \text{ keV}$ while the plasma sheet ions have $T=1 \text{ keV}$. All flow velocities are assumed zero. The effect of photon statistics on the image quality indicates a maximum of 48 counts for a given pixel at the detector.

appear relatively bright. The maximum image brightness is given by 3.74×10^{-4} , 3.78×10^{-4} , 3.99×10^{-4} and 4.19×10^{-4} Rayleighs, respectively. For positive (sunward) drift velocities the images obtained for the various flow speeds and their scattering rates in photons/s/ion are shown in Fig. 5 frame (a) $v_p = 100 \text{ km s}^{-1}$, $g = 1.7 \times 10^{-7}$ (b) $v_p = 200 \text{ km s}^{-1}$, $g = 2.5 \times 10^{-7}$ (c) $v_p = 300 \text{ km s}^{-1}$, $g = 2.6 \times 10^{-7}$ (d) $v_p = 400 \text{ km s}^{-1}$, $g = 1.4 \times 10^{-7}$. Frame (a) show a dim image of the plasma sheet while frames (b) and (c) show enhanced brightness of the plasma sheet as reflected from the relative values of the scattering rates. The maximum image brightness obtained is given by 3.60, 3.73, 3.74 and 3.55 times 1×10^{-4} Rayleighs, respectively.

Temperature Variations

The survey of the plasma sheet ion composition done by (Lennartson et al., 1986) indicated an average O^+ ion number density of $.1 \text{ cm}^{-3}$. However, their instrument selected ion energies in the keV range excluding any 'cold ions' in their results. Hence, we have no direct evidence of the cold ion density. We fixed the plasma sheet temperature at 1 keV and allow the plasma temperature to vary in the radiation belt. The flow velocities are assumed to be zero. The results of the simulations are shown in Fig. 6 for Case 2 where frame (a) $T = 1 \text{ keV}$ (b) $T = 4 \text{ keV}$ (c) $T = 8 \text{ keV}$ (d) $T = 10 \text{ keV}$. The scattering rates calculated for the radiation belt are 2.45, 2.57, 2.69 and 2.67 times 1×10^{-7} photons/s/ion, respectively. The image brightness is almost constant for temperature variations from $T = 1 \text{ keV}$ to $T = 10 \text{ keV}$. Our simulations indicate the maximum intensities to be 3.24, 3.38, 3.51 and 3.49 times 1×10^{-4} Rayleighs, respectively for the four frames above.

Imaging the Radiation Belt and Plasma Sheet

One of the objectives of the above analysis is to determine the feasibility of imaging the magnetosphere in the scattered light of O^+ . A useful way to summarize the results is to calculate the size of the collecting aperture needed to image the magnetosphere under various circumstances. Assuming a substorm time scale of 1 hour, we shall adopt 1000 sec as a minimal time resolution. The camera is assumed to employ spectrally selective multilayer mirrors of sufficiently narrow passband that no further filtering is required. (Recent work by Seeley, (private communication) show that this is likely to admit an unacceptable amount of Lyman α contamination). We further assumed an optical transmission of 30% and a detector counting efficiency of 10%, giving an overall system efficiency of 3%.

Using a realistic value of 10 keV for the temperature of the ions in the radiation belt and a plasma sheet temperature of 1 keV, a simulation image was performed for the view direction given by Case 4 using an aperture of 750 cm^2 . A randomized image using Poissonian statistics is shown in Fig. 7 demonstrating the expected quality for the particular instrument parameters.

5. POSSIBLE CONTRIBUTIONS FROM O^{++} IONS

The global images of the magnetosphere that we have obtained depended solely on contributions from the O^+ ions. Contributions from the O^{++} ions have been neglected. Results of a model calculation by (Chandler, 1987) suggest that the O^{++} density is about a factor 20 lower than the O^+ density. However, under certain solar and magnetospheric conditions, if the O^{++} number density becomes comparable to that of O^+ it can contribute to an overall larger emission rate.

CONCLUSION

We have investigated the effects of Doppler shifting on the line centers of the magnetospheric O^+ cross-section and explained the resulting structure of the scattering rate as a function of bulk velocity. Whereas the Doppler shifting frequently results in a decrease of the scattering rate, it has been demonstrated that for certain drift speeds, the overlap of the cross-section and the solar intensity profile can lead to an increased rate thus enhancing the relative brightness of the image above that obtained when v_p is zero.

Using a dipole field configuration for the magnetic field and a simple model of the O^+ number density profile we are able to obtain simulated images of the magnetosphere and show quantitatively how the magnetospheric image responds to variations in plasma drift speed and temperature. Changes in the brightness of the magnetospheric images will also depend on the variability of the solar flux at 834 nm. Assuming a fixed temperature, in regions where there are plasma drifts the brightness in the image is governed by the structure of the scattering rate.

To illustrate how an instrument would respond to a typical magnetospheric source brightness we have shown a randomized image of the radiation belt and plasma sheet. This demonstrates that gross features of those regions can be seen using a camera aperture of at least 750 cm^2 .

Acknowledgements. This work was supported in part by NASA grants NAGW 1520 and 1787 and funds from the Geophysical Institute, University of Alaska, Fairbanks.

We would like to thank Richard Guritz and Joanne Grooves for their help in producing the images using the University of Alaska Data Visualization and Analysis Laboratory facility.

The authors thank David Kula (University of Alaska summer intern, 1989) for his calculations of scattering efficiency.

The authors also thank the referees for their suggestions in revising this paper.

REFERENCES

- Blake, I.F., Application to Applied Probability, Wiley and Son's 1979.
- Chiu, Y.T., Robinson, R.M., and Colin, H.L. (1990) Magnetospheric and Exospheric Imaging In The Extreme Ultraviolet, Geophys. Res. Lett., Vol. 17, No. 3, p. 267.
- Chiu, Y.T., Robinson, R.M., Swenson, G.R., Chakrabarti, S.S., and Evans, D.S. (1986) Imaging The Outflow of Ionospheric ions into the Magnetosphere, Vol. 322, p. 31.
- Chandler, Kosyra, J.U., Horwitz, J.L., Comfort R.H., and Brace, L.H. (1987) Modeling of the Thermal Plasma in the Outer Plasmasphere - A Magnetospheric Heat Source, (Geophysica Monograph 44, Modeling Magnetospheric Plasma, Edited by Moore, T.E., et. al.).
- Hess, W.N., The Radiation Belt and Magnetosphere, Blaisdell Publishing Company, 1968.
- Hinteregger, H.E., Fukui, K., and Gilson, B.R. (1981) Observational, Reference and Model Data on Solar EUV, From Measurements on AE, E, Geophys. Res. Lett., 8, p. 1147.
- Ho, Y.K. and Henry, R.J.W. (1983) Oscillator Strengths and Collision Strengths for OII and OIII, Astrophys. J., 264, p. 733.
- Johnson, C.Y., Young, J.M., and Holmes, J.C. (1971) Magnetoglow - a New Geophysical Resource, Science, 171, p. 379.
- Kumar, S., Chakrabarti, S.S., Pearce, F., and Bowyer, S. (1983) The O+ 834 A Dayglow: Satellite Observations and Interpretation with a Radiation Transfer Model, J. Geophys. Res., 88, p. 9271.
- Lennartson, W. and Shelley, E.G. (1986), Survey of .1-16 keV/e Plasma Sheet Ion Composition, J. Geophys. Res., 91, 3061.
- Meier, R.R. (1990a) The Scattering Rate of Solar 834 A Radiation By Magnetospheric O^+ and O^{++} , Geophys. Res. Lett., vol. 17, p. 1613.

Meier, R.R., Widing, K.G., and Feldman, U. (1991) Analysis of the Solar OII/OIII Multiplets at 834 Å: Implications for the Emission Measure Distribution in the Vicinity of 40000 K, *Astrophys. J.*, vol. 369, p. 570.

Meier, R.R., Ultraviolet Spectroscopy and Remote Sensing of the Upper Atmosphere, *Space Sci. Rev.*, submitted for publication, 1990b.

Rees, M.H., *Physics and Chemistry of the Upper Atmosphere*, Cambridge University Press, 1989.

Roederer, J., *Dynamics of Geomagnetically Trapped Radiation* Springer-Verlag, 1970.

Roelef, E.C. (1989) Remote Sensing of the Ring Current Using Energetic Neutral Atoms, *Adv. Space Res.*, Vol. 9, No. 12 pp(12)195-(12)203.

Swift, D.W., R.W. Smith., S.-I. Akasofu (1989) Imaging The Earth's Magnetosphere, *Planet. Space Sci.*, 37, No. 4, p. 379.

Timothy, J.G. (1977) The solar spectrum between 300 and 1200 Å, in *Solar Output and its Variation* (Edited by White, O.R.), p. 237. Colorado Associated University Press, Boulder.

APPENDIX: ANALYSIS OF THE CROSS SECTION

Because of the ion's thermal speed, the absorption cross-section of a hot plasma containing O^+ ions for a particular line transition will be broadened. Consider an O^+ ion with a temperature T_i and mass m_o . It will have a thermal speed

$$u_i = \sqrt{2kT_i/m_o} \quad (A-1)$$

If ν_{oi} is the frequency of radiation emitted by a stationary source then the frequency of radiation absorbed in the rest frame of the ion is given by

$$\nu = \nu_{oi}(1 + v/c) \quad (A-2)$$

The absorption cross-section is assumed to have a gaussian form

$$\sigma_i^a = c_i e^{-\frac{x^2}{\nu_{oi}^2}} \quad (A-3)$$

Solving for the velocity in (A-2), we get

$$\sigma_i^a(\nu) = \sum_i c_i e^{-\frac{c^2}{\nu_{oi}^2}(\nu - \nu_{oi})^2} \quad (A-4)$$

where the constants c_i are obtained as follows; from (Rees, 1989), we use the following expressions

$$\sigma_i^a(\nu) = \frac{c^2}{8\pi} \frac{w_u}{w_l} \frac{1}{\nu^2} A_{lu}^i \phi_i(\nu) \quad (A-5)$$

where

$$\int_{-\infty}^{\infty} \phi_i(\nu) d\nu = 1 \quad (A-6)$$

w_u and w_l are statistical weights of the upper and lower levels for a particular transition and $\phi_i(\nu)$ is the normalized spectral intensity distribution. A_{lu} is the Einstein coefficient for the transition from upper to lower levels. The normalization for σ_i^a is given by

$$\int_0^{\infty} \sigma_i^a d\nu = \frac{\pi e^2}{m_e c} f_i \quad (A-7)$$

where (f_i) is the oscillator strength for the emission of radiation with frequency ν_{oi} . We can obtain A_{lu} by requiring (A-6) to be satisfied ie.

$$\int_{-\infty}^{\infty} \frac{c^2}{8\pi} \frac{w_u}{w_l} \frac{A_{lu}}{\nu^2} \frac{m_e c}{\pi e^2 f_i} \phi_i(\nu) d\nu = 1 \quad (A-8)$$

to get

$$A_{lu} = \frac{\pi e^2}{m_e c} f_i \frac{8\pi}{c^2} \frac{w_l}{w_u} \nu^2 \quad (A-9)$$

Now, using (A-9) into (A-5) we get the result

$$\sigma_i^a(\nu) = \sigma_i \phi_i(\nu) \quad (A-10)$$

where

$$\sigma_i = \frac{\pi e^2}{m_e c} f_i \quad (A-11)$$

Our absorption cross-section profile can then be expressed as a sum of the individual profiles composed of O^+ transitions belonging to the 83.4 nm band. Hence,

$$\sigma^a(\nu) = \sum_i \sigma_i \phi_i(\nu) \quad (A-12)$$

with

$$\phi_i(\nu) = \kappa_{oi} e^{-\frac{c^2}{\nu_{oi}^2}(\nu - \nu_{oi})^2} \quad (A-13)$$

Normalising $\phi_i(\nu)$ we get

$$\kappa_{oi} = \frac{c}{u_i \nu_{oi} \sqrt{\pi}} \quad (A-14)$$

Finally, the absorption cross-section profile is given by

$$\sigma^a(\nu) = \sum_{i=1}^3 \sigma_i \kappa_{oi} e^{-\frac{c^2}{\nu_{oi}^2}(\nu - \nu_{oi})^2} \quad (A-15)$$

The absorption cross-section at line center is then given by the expression $\sigma_{oi} = \sigma_i \kappa_{oi}$ which specifies the constants c_i . When a parcel of plasma is drifting with a bulk velocity v_p relative to the emitting source, the frequency center of the cross-section profile is shifted by an amount

$$\nu_i = \nu_{oi}(1 + v_p/c).$$

The Doppler shifted cross-section can now be expressed as

$$\sigma_d^a(\nu) = \sum_{i=1}^3 \sigma_i \kappa_{oi} e^{-\frac{c^2}{\nu_{oi}^2}(\nu - \nu_i)^2} \quad (A-16)$$

CALCULATION OF THE SCATTERING RATE

The scattering rate (photons/sec/ion) or the g-factor is calculated from the expression

$$g(v_p) = \int_{-\infty}^{\infty} \sigma_d^a(v_p, \nu) I(\nu) d\nu \quad (A-17)$$

Using expressions (7),(8) and (A-16),

$$g = \sum_n \sum_m I_n \kappa_{on} \sigma_m \kappa_{om} Q_{nm} \quad (A-18)$$

where

$$Q_{nm} = \int_{-\infty}^{\infty} e^{-\delta_{nm} \nu} d\nu \quad (A-19)$$

and

$$\delta_{nm} = c_1^2(\nu_{0n} - \nu)^2 + c_2^2(\nu_m - \nu)^2 \quad (A-20)$$

$$c_1^2 = \frac{c^2}{\nu_{0n}^2 u_n^2} \quad (A-21)$$

$$c_2^2 = \frac{c^2}{\nu_{0m}^2 u_m^2} \quad (A-22)$$

The indices m and n refer to magnetospheric and solar quantities respectively. We can simplify δ_{nm} in a form that allows us to integrate Q_{nm} easily, ie.

$$\delta_{nm} = \gamma_0 - \beta\nu + \alpha\nu^2 \quad (A-23)$$

where

$$\gamma_0 = c_1^2 \nu_{0n}^2 + c_2^2 \nu_m^2 \quad (A-24)$$

$$\beta = 2(c_1^2 \nu_{0n} + c_2^2 \nu_m) \quad (A-25)$$

$$\alpha = c_1^2 + c_2^2 \quad (A-26)$$

Integrating Q_{nm} gives us the result

$$Q_{nm} = \sqrt{\frac{\pi}{\alpha}} e^{\frac{(\beta^2 - 4\alpha\gamma_0)}{4\alpha}} \quad (A-27)$$

Further simplification leads to the following result

$$\sqrt{\frac{\pi}{\alpha}} = \frac{1}{\kappa_{0m} \sqrt{A}} \quad (A-28)$$

$$A = \frac{\nu_{0m}^2 u_m^2}{\nu_{0n}^2 u_n^2} + 1 \quad (A-29)$$

We can finally express g as

$$g = \sum_n \sum_m I_n \sigma_m \frac{\kappa_{0n}}{\sqrt{A}} e^{-t_r} \quad (A-30)$$

with

$$\delta_p = \frac{c^2(\nu_m^2 - 2\nu_{0n}\nu_m + \nu_{0n}^2)}{(\nu_{0m}^2 u_m^2 + \nu_{0n}^2 u_n^2)} \quad (A-31)$$